*applied sciences*

MDPI

*Article*

# Assessing the Pisano Equations for Dry-Weather Solids Deposition in Sewer Systems: Comparative Behavior and Sensitivity Analysis

**José Bravo Márquez [1], F. Javier Marín-Rodríguez [2], José Manuel Poyatos Capilla [1,3] and Jaime Martín-Pascual [1,3,*]**

[1] Department of Civil Engineering, University of Granada, Campus Universitario de Fuentenueva, 18071 Granada, Spain; jose5400@correo.ugr.es (J.B.M.); jpoyatos@ugr.es (J.M.P.C.)
[2] Department of Applied Mathematics, Materials Science and Engineering, and Electronic Technology, Rey Juan Carlos University, Calle Tulipán s/n, Móstoles, 28933 Madrid, Spain; javier.marin@urjc.es
[3] Institute of Water Research, University of Granada, 18071 Granada, Spain
* Correspondence: jmpascual@ugr.es

## Featured Application

Auditing historical deposition surrogates and standalone screening equations under explicitly stated synthetic input designs.

## Abstract

Four historical Pisano power-law equations for daily dry-weather solids deposition are audited using transparent numerical and analytical diagnostics. EQ1 is an endogenous surrogate: its slope descriptors depend on prior modeled deposition, whereas EQ4 can be evaluated from standalone network-scale inputs. An independent-uniform exploration of historical input ranges, rather than real-world occurrence probabilities, uses a common Latin hypercube sample of 200,000 combinations and gives median deposited-solids masses of 34.9, 168.0, 164.5, and 159.2 kg day$^{-1}$ for EQ1–EQ4. The paired EQ1/EQ4 median log-ratio is −0.622, so EQ1 is the lower formulation. However, 19.7% of these unconstrained baseline combinations violate slope-descriptor ordering. Additional designs enforce ordering, a field-informed length-to-area envelope, and, separately, linked exponential slope quantiles. EQ1 remains distinct in these constrained tests, but its EQ4 log-ratio changes to −0.688, −0.711, and −0.422, respectively. High global rank correlations do not imply tail interchangeability: baseline EQ1/EQ4 and EQ2/EQ4 top-decile overlaps are 21.6% and 76.2%. Elasticities are invariant model properties, whereas variance shares depend on bounds and dependence: narrowing the length interval makes the EQ1 slope descriptor outweigh length. Under log-uniform marginals, output medians nearly coincide; retaining the four original flow levels also changes the induced distributions. All reported distributions and sensitivity rankings are conditional on these explicitly assumed designs. These findings support a conditional mathematical comparison of a model-dependent surrogate with standalone screening equations; they do not establish physical dominance, predictive equivalence, or design suitability.

**Keywords:** sewer sediments; dry-weather deposition; Pisano equations; Latin hypercube sampling; global sensitivity analysis; partial rank correlation; uncertainty characterization

Check for updates

Academic Editor: Francisco Heras

Received: 27 September 2026
Revised: 22 October 2026
Accepted: 28 October 2026
Published: 31 October 2026

**Copyright:** © 2026 by the authors. Licensee MDPI, Basel, Switzerland. This article is an open access article distributed under the terms and conditions of the Creative Commons Attribution (CC BY) license.

## 1. Introduction

The accumulation of solids in sewer systems poses significant hydraulic and environmental challenges. Deposited sediment reduces conveyance capacity, increases maintenance requirements, and acts as a reservoir of pollutants that can be mobilized during rainfall events [1,2]. Deposition is inherently dynamic because hydraulic conditions and the characteristics of incoming solids vary continuously across space and time [2,3].

During dry-weather periods, low flow velocities often fail to maintain particles in suspension, promoting gradual settling on the pipe bed [2,4]. This phenomenon is particularly critical in combined sewer networks, where pipe geometry—including slope, diameter, and spatial configuration—dictates where accumulation occurs [1,4]. Sediment transport and settling are further governed by physical properties, such as particle-size distribution, organic content, and cohesive behavior, which dictate both initial deposition and resistance to subsequent erosion [5,6].

Accumulated dry-weather deposits represent temporary in-sewer pollutant storage [1,2]. During subsequent storm events, increased shear stress resuspends these solids, contributing significantly to the "first flush" phenomenon, in which high concentrations of pollutants are mobilized early in the hydrograph [6,7]. Dry-weather deposition is thus a primary mechanism linking antecedent dry periods to wet-weather pollution released via combined sewer overflows or delivered to treatment facilities [1,7].

Solids entering urban drainage systems originate both from wastewater and urban surface runoff [1,2]. Evaluating and managing these accumulated loads requires effective modeling tools. Detailed numerical models represent deposition processes explicitly but require calibration and extensive hydraulic and sediment characterization [2,6]. Empirical formulations, by contrast, estimate deposition from a limited set of geometric and operational parameters, making them practical screening tools for network-scale assessments [8,9].

Contemporary evidence places these aggregate screening equations within a much broader process framework. Wastewater-fed pipe experiments by Regueiro-Picallo et al. [10] showed that deposition duration and biological transformations alter the cohesion and erosion threshold of organic deposits. More recently, Tang et al. [11] examined how food-waste inputs modify extracellular polymeric substances and sediment erosion resistance during prolonged incubation. Such experiments concern bed evolution and erodibility, so they motivate transferability limits rather than independently validating a daily network-scale deposition formula.

Field evidence also extends beyond geometry alone. Using Kyoto sewer records from 2014 to 2023, Liu et al. [12] related accumulation to interacting environmental and wastewater-quality factors, with different associations across channel structures and junctions. Complementary hydraulic experiments and modeling by Yang et al. [13] distinguish continuous sediment beds from local obstructions and show that different deposition patterns can produce similar overall energy losses. These findings explain why a total-length effect in an aggregate equation cannot identify the location, hydraulic consequence, or physical cause of an observed deposit.

Methods for observing and predicting deposits have also developed. Temperature-based approaches combine sediment thermal properties with heat-transfer analysis to estimate bed depth [14,15]. A two-stage machine-learning approach instead combines pipe characteristics with rainfall and maintenance information to classify future deposition thresholds [16]. These targets—local bed depth or threshold classes—differ from daily deposited-solids mass. The present audit complements these approaches by testing the mathematical consistency and information requirements of four historical surrogates; it does not benchmark their predictive skill against contemporary monitoring or learning methods.

A foundational effort in this domain was conducted by Pisano et al., who investigated dry-weather deposition and flushing strategies in combined sewers [7]. Building on this work, Pisano and co-workers proposed four empirical formulations of increasing simplicity to estimate daily deposited-solids masses from basic physical and hydraulic parameters [8]. These formulations trade data requirements against model complexity, offering choices ranging from detailed slope-distribution metrics to basic network dimensions.

Despite their age, the applicability of the Pisano formulations remains relevant. Later studies have shown that local conditions can substantially affect sediment accumulation and the transferability of empirical deposition estimates to other sewer systems [6,9]. Trapote and Egea [9], in particular, applied the Pisano model to catchments in semi-arid regions and found marked differences between estimated and measured loads, highlighting the influence of antecedent dry periods and system-specific characteristics. However, the comparative behavior of the four formulations across their original input domains remains insufficiently characterized. In particular, it is unclear how strongly their predictions differ, whether they rank sewer-system scenarios consistently, which input variables dominate their responses, and whether the additional information required by the more complex formulations translates into materially different model behavior. Addressing these questions is relevant when empirical equations are used for preliminary assessment under limited network characterization.

The contribution of this paper is a systematic mathematical audit of all four Pisano formulations within one paired input-space exploration, combining analytical invariants with distribution-dependent magnitude, ranking, and sensitivity diagnostics. This differs from applying a single formulation to a catchment and addresses their joint behavior without asserting predictive superiority. We define $M_{\mathrm{SpTS}}$ as the estimated daily dry-weather deposited total-solids mass per unit time (kg day$^{-1}$) under the historical clean-pipe assumptions. It is not the existing bed stock (kg), an incoming wastewater solids load, or an event export. The term "daily deposited-solids mass" is used for this model output below. Specifically, this study assesses the following:

1. **Output magnitude and scale disagreement:** evaluated through median daily deposited-solids masses and pairwise log-ratios ($R_{ij}$);
2. **Scenario-ranking consistency:** measured using Spearman and Kendall rank correlations, top-decile overlap, and large percentile-rank shifts;
3. **Variable sensitivity and mathematical controls:** characterized by partial rank correlation coefficients (PRCCs), exact logarithmic variance shares ($S_{\log}$), deterministic range effects, and upper-tail input profiles ($U_{k,v}$);
4. **Response structure and data parsimony:** contrasting the most complex slope-distribution model against simpler macro-variable formulations to evaluate data-burden trade-offs.

By separating internal mathematical response from empirical validation, this analysis tests which comparisons survive explicit input restrictions and which ones depend on the synthetic sampling design. No equation is selected on predictive accuracy.

## 2. Materials and Methods

### *2.1. Historical Basis, Formulations, and Input Domain*

The four formulations estimate $M_{\mathrm{SpTS}}$ as defined above, with the same mass basis and historical assumptions throughout the audit. They were originally fitted to deposition-model outputs rather than directly to measured network-wide deposits. The calibration comprised 75 sewer basins evaluated at four per-capita wastewater-flow levels under an assumed clean-pipe condition and a fixed solids contribution of 0.5 lb person$^{-1}$ day$^{-1}$ (approximately 0.227 kg person$^{-1}$ day$^{-1}$) [4,8]. This provenance is important: the equations are

historical screening surrogates for the original deposition model and are not contemporary observational laws.

Appendix B supplies the US customary forms at the audited exponent precision, a worked conversion, and same-input numerical checks. The original equations used pounds per day for the output, feet for pipe length, acres for service area, inches for diameter, and gallons per capita per day for wastewater flow. The present analysis used the corresponding rounded SI forms:

$$M_1 = 2.64 \times 10^{-4} L^{0.814} S_{PD}^{-0.819} S_{PD/4}^{-0.108} d^{-0.510}, \quad (1)$$

$$M_2 = 10.91 \times 10^{-4} L^{1.180} A^{-0.178} S^{-0.418} D^{0.604} d^{-0.510}, \quad (2)$$

$$M_3 = 3.69 \times 10^{-4} L^{1.220} A^{-0.187} S^{-0.434} d^{-0.510}, \quad (3)$$

$$M_4 = 7.09 \times 10^{-4} L^{1.063} S^{-0.438} d^{-0.510}. \quad (4)$$

Here, $L$ is the total pipe length, $A$ is the service area, $S$ is the mean pipe slope, $D$ is the mean equivalent pipe diameter, and $d$ is the per-capita wastewater flow including infiltration. The descriptor $S_{PD}$ is the pipe slope corresponding to $P_{LD}$, where $P_{LD}$ denotes the percentage of total pipe length over which 80% of the modeled deposited load occurs. The descriptor $S_{PD/4}$ is the slope at one quarter of that cumulative pipe-length percentage. Thus, $S_{PD/4}$ is not a fourth moment or a fourth-power term; it is a lower-tail slope-distribution descriptor defined by the original procedure [4,8].

EQ1 therefore has endogenous inputs in the operational sense that its descriptors incorporate prior deposition-model output through $P_{LD}$. They cannot be obtained from network geometry alone without additional model-based information or a justified approximation to the original procedure. EQ1 is a surrogate conditional on that information, not a standalone prospective predictor. EQ4, by contrast, requires only $L$, $S$, and $d$. Appendix A and Figure A1 illustrate how the prior deposition output supplies $P_{LD}$ and how the geometry-derived slope distribution then supplies the two quantiles. This distinction does not assert econometric endogeneity of an error term; it identifies the information dependence of the inputs.

The SI coefficients were obtained by transforming the empirical coefficients together with their input units. In general, if $x_{v,\mathrm{US}} = c_v x_{v,\mathrm{SI}}$ and $m_{\mathrm{kg}} = c_m m_{\mathrm{lb}}$, then

$$C_{k,\mathrm{SI}} = c_m C_{k,\mathrm{US}} \prod_{v \in U_k} c_v^{\alpha_{k,v}}. \quad (5)$$

Table 1 specifies all conversion factors, and Table 2 distinguishes reconstructed coefficients from the fixed rounded SI coefficients audited here. Keeping the rounded exponents in Equations (1)–(4), conversion of the historical US coefficients gives small differences (at most 0.24%) from the supplied SI forms. We therefore do not claim exact recovery at the displayed precision. The audited coefficient vector is explicitly fixed; changing coefficient rounding would alter magnitudes slightly but not elasticities, variance shares, or ranks. Converting inputs while retaining unconverted US coefficients would be inconsistent.

Table 3 reports the explored bounds, obtained by converting the ranges of the original regression inputs. The original wastewater-flow regressor took four discrete values (40, 110, 190, and 260 gallons per capita per day); the present design explores the continuous interval between its converted endpoints. All slope variables are dimensionless. The explored lower bounds $S_{PD} = 0.0011$ and $S_{PD/4} = 0.000089$ are both strictly positive. No negative inputs are sampled, shifted, replaced with absolute values, or clipped before evaluating fractional powers or logarithms. Positivity is checked in the supplied script. The table defines the

adopted historical-range envelope; its Cartesian product is not itself a physically admissible calibration dataset.

**Table 1.** Unit conversion convention: $x_{\mathrm{US}} = c_v x_{\mathrm{SI}}$; output mass uses $m_{\mathrm{kg}} = c_m m_{\mathrm{lb}}$.

| Quantity | Exact Unit Relation | Factor Used |
|---|---|---|
| $L$ | 1 ft = 0.3048 m | $c_L = 1/0.3048$ |
| $A$ | 1 acre = 0.40468564224 ha | $c_A = 1/0.40468564224$ |
| $D$ | 1 in = 0.0254 m | $c_D = 1/0.0254$ |
| $d$ | 1 US gal = 0.003785411784 $m^3$ | $c_d = 1/0.003785411784$ |
| $S, S_{PD}, S_{PD/4}$ | ft/ft = m/m | $c_S = c_{PD} = c_{PD/4} = 1$ |
| Mass | 1 lb = 0.45359237 kg | $c_m = 0.45359237$ |

**Table 2.** Coefficient audit using the rounded exponents printed in this article and US coefficients from Pisano and Queiroz [4], Section 4.5.3. The final column gives $(C_{\mathrm{converted}}/C_{\mathrm{audited}} - 1) \times 100$. The audited SI column is the coefficient vector used in all calculations.

| | Historical $C_{\mathrm{US}}$ | Converted $C_{\mathrm{SI}}$ | Audited $C_{\mathrm{SI}}$ | Difference (%) |
|---|---|---|---|---|
| EQ1 | 0.0038 | 0.000263815 | 0.000264 | −0.070 |
| EQ2 | 0.001303 | 0.001093598 | 0.001091 | +0.238 |
| EQ3 | 0.00389 | 0.000369391 | 0.000369 | +0.106 |
| EQ4 | 0.0076 | 0.000709266 | 0.000709 | +0.038 |

**Table 3.** Input variables and bounds used in the input-space exploration.

| Variable | Description | Unit | Minimum | Maximum |
|---|---|---|---|---|
| $L$ | Total pipe length | m | 80.16 | 41,004.13 |
| $A$ | Service area | ha | 1.214 | 259.404 |
| $S$ | Mean pipe slope | – | 0.00238 | 0.0799 |
| $D$ | Mean equivalent pipe diameter | m | 0.2032 | 0.5080 |
| $S_{PD}$ | Slope at cumulative pipe-length percentage $P_{LD}$ | – | 0.0011 | 0.0589 |
| $S_{PD/4}$ | Slope at cumulative pipe-length percentage $P_{LD}/4$ | – | 0.000089 | 0.0249 |
| $d$ | Per-capita wastewater flow, including infiltration | $m^3$ $person^{-1}$ $day^{-1}$ | 0.1514 | 0.9842 |

All four equations are multiplicative power-law models and can be expressed as

$$M_k = C_k \prod_{v \in \mathcal{V}_k} x_v^{\alpha_{k,v}}, \tag{6}$$

where $C_k$ is the coefficient of equation $k$, $\mathcal{V}_k$ is its input set, $x_v$ is the value of input $v$, and $\alpha_{k,v}$ is the corresponding empirical exponent. Taking base-10 logarithms gives the exact additive representation

$$Y_k \equiv \log_{10}(M_k) = \log_{10}(C_k) + \sum_{v \in \mathcal{V}_k} \alpha_{k,v} \log_{10}(x_v). \tag{7}$$

This representation facilitates comparison across several orders of magnitude and permits analytical attribution of log-output variance.

### 2.2. Sampling Designs, Constraints, and Reproducibility

All baseline comparisons use one common seven-column randomized Latin hypercube sample (LHS), $N = 200{,}000$, generated by `scipy.stats.qmc.LatinHypercube` with seed 123 and columns ordered as $L, A, S, D, S_{PD}, S_{PD/4}, d$. The baseline (B) uses independent continuous uniform marginals within the bounds in Table 3. Selecting an equation's columns preserves each column's LHS stratification; equation-specific samples are unnecessary for that purpose. Finite-sample correlations can occur, but the target baseline distribution is a product distribution. The four historical discrete flow levels are replaced in B by their continuous endpoint interval; this is an interpolation experiment, not the original regression experiment. Design F tests this choice explicitly: the other six B columns are retained, while the seventh unit-cube coordinate selects 40, 110, 190, or 260 US gal person$^{-1}$ day$^{-1}$ with equal weights. Exact conversion gives 0.151416, 0.416395, 0.719228, and 0.984207 m$^3$ person$^{-1}$ day$^{-1}$. Each level occurs 50,000 times. Equal weights reproduce the four-level experimental structure, not an observed flow-frequency distribution. Appendix C reports medians, ranks, tail overlaps, PRCCs, and exact mixed-distribution log-variance shares.

LHS is used for paired rankings, tail membership, and induced output distributions, which are not specified by exponents alone. Elasticities, endpoint effects, and independent log-variance shares are calculated analytically. The simulation is not used to numerically estimate quantities already available in closed form. Checks at $N = 10{,}000$, 50,000, and 200,000, with seeds 123–125, are supplied. At $N = 200{,}000$, EQ1 and EQ4 medians span 34.87–34.94 and 158.88–159.24 kg day$^{-1}$; their top-decile overlap spans 0.216–0.225. These are numerical replication ranges, not confidence intervals for real networks. Appendix D presents all nine sample-size/seed checks in a readable table and in CSV form.

Because cumulative slope quantiles are ordered, a second design (O) rejects rows unless $S_{PD/4} \le S_{PD}$. Design C applies the same ordering and also restricts sewer density $L/A$ to 60.389–278.076 m ha$^{-1}$, the minimum and maximum computed from the eight networks in Table 1 of Trapote and Egea [9]. This envelope supplies a transparent, field-informed length–area constraint, rather than an invented population correlation. It is illustrative and does not establish a universal design rule.

Design E strengthens the slope consistency check by assuming that the length-weighted pipe-slope distribution is exponential, a historical approximation considered by Pisano and Queiroz [4]. From a latent $p \sim U(0,1)$ and mean slope $S$, define

$$S_{PD} = -S\ln(1-p), \qquad S_{PD/4} = -S\ln(1-p/4). \tag{8}$$

Reject rows outside the two descriptor bounds and the same density envelope. This produces ordered quantiles of a common distribution with mean $S$. The latent $p$ represents a possible cumulative length fraction; it is not recomputed from deposited-load allocation. Thus, E is a geometry-consistent surrogate stress test, not a reconstruction of the endogenous $P_{LD}$ procedure or a validated distribution of real sewers. No slope–diameter rule or full network hydraulic feasibility is asserted.

For O, C, and E, successive seven-dimensional LHS batches of 200,000 proposals use seeds $223 + b$, $323 + b$, and $423 + b$, respectively, where $b = 0, 1, \ldots$. Accepted rows are concatenated in proposal order and the first 200,000 are retained. For E, the fifth unit-cube coordinate supplies $p$ and the sixth is unused; the other coordinates retain their stated marginals before rejection. Accepted samples are no longer LHS and their marginals change. Batch acceptance rates are 80.28%, 42.40%, and 38.32%; two, three, and three batches are needed. The restricted designs satisfy their specified constraints, but no set of a few aggregate inequalities guarantees full physical network admissibility.

Bounds robustness is assessed without extrapolation. Let $g_v = \sqrt{a_v b_v}$ and $r_v = b_v/a_v$. Replacing $[a_v, b_v]$ with $[g_v/r_v^{1/4}, g_v r_v^{1/4}]$ retains the central half of its logarithmic width. H applies this to all inputs, HL only to $L$, and HP only to $S_{PD}$. G uses independent log-uniform marginals on the original endpoints. H, HL, HP, and G retain the same seed and seven-dimensional unit-cube sample as B. These unconstrained alternatives isolate bounds or marginal-distribution effects; they are not additional physically admissible designs.

All numerical results and figures use the documented common-sample workflow implemented in the reproducibility code. Appendices A–E provide the additional methods and checks within this article. The procedural source code, environment manifest, and derived CSV tables are publicly available in the GitHub repository described in Appendix E. The design follows the stratified-sampling rationale of McKay et al. [17] and Helton et al. [18,19]. The numerical environment was Python 3.12.14, NumPy 2.3.5, SciPy 1.17.0, pandas 2.2.3, and Matplotlib 3.10.8. No field observations are generated by the simulation.

### 2.3. Comparison of Equation Outputs

For every common-sample row, $M_1$–$M_4$ and their logarithms $Y_k = \log_{10}(M_k)$ were calculated. Normalized histograms of $Y_k$ compare the output distributions induced by each synthetic design; their densities do not represent occurrence probabilities in real sewer populations. Medians were reported on the original kg day$^{-1}$ scale.

Magnitude disagreement between equations $i$ and $j$ was quantified by the paired log-ratio

$$R_{ij} = \log_{10}\left(\frac{M_i}{M_j}\right) = Y_i - Y_j. \tag{9}$$

Thus, $R_{ij} = 0$ denotes equal outputs, $R_{ij} = 1$ a tenfold larger output from equation $i$, and $R_{ij} = -1$ a tenfold smaller output. Analyzing paired differences is a standard way to distinguish agreement in magnitude from association [20].

Scenario-ranking consistency was assessed using Spearman's rank correlation,

$$\rho_{ij}^S = \rho_S(Y_i, Y_j), \tag{10}$$

which measures whether two equations order the sampled rows similarly regardless of absolute scale [21].

Kendall's $\tau_b$ is also reported. For top-decile agreement, let $\mathcal{D}_k$ contain exactly the highest $n_{10} = 20{,}000$ outputs, using stable row order to break any ties. We use

$$O_{ij}^{(10)} = \frac{|\mathcal{D}_i \cap \mathcal{D}_j|}{n_{10}}. \tag{11}$$

This is common-tail membership (not a Jaccard index); random independent membership has expected overlap 0.10. To locate large reorderings, $q_k(s) = \text{rank}[M_k(s)]/N$ and $\delta(s) = q_1(s) - q_4(s)$ define groups with $\delta \geq 0.5$ and $\delta \leq -0.5$. Input medians are reported for each group and the 100 largest absolute shifts are supplied.

Log-ratios and rank correlations therefore answer different questions: the former quantify magnitude disagreement, whereas the latter quantify consistency in the ordering induced by the synthetic design.

### 2.4. Variable Sensitivity Analysis

Input influence was evaluated using PRCCs and an analytical decomposition of log-output variance. These measures are well suited to deterministic, monotonic power-law equations: PRCC describes the direction and strength of a conditional monotonic association, while the variance share attributes output variability under the adopted input distributions [19,22–24].

For equation $k$, all inputs and $Y_k$ were first rank-transformed. The ranked input $x_v$ and ranked output were separately regressed on the remaining ranked inputs. The PRCC was the Pearson correlation between the residuals,

$$\mathrm{PRCC}_{k,v} = \mathrm{corr}\left(\varepsilon_{x_v}, \varepsilon_{Y_k}\right). \tag{12}$$

Values range from −1 to 1. The sign indicates the direction of the association, and the absolute value indicates its conditional monotonic strength. For independent inputs, the monotonic signs are already known from the exponents; PRCC adds no new structural sign information. We retain it as a descriptive check of conditional rank association and of changes under joint restrictions. It complements exact variance attribution and endpoint effects by addressing ranked sample responses, but it is not an independent validation of the equations or a substitute for their analytical elasticities. With $N = 200{,}000$, inferential $p$-values would be dominated by sample size; interpretation therefore focuses on effect magnitude and direction.

Because Equation (7) is additive and the sampled inputs are independent, the contribution of input $v$ to $\mathrm{Var}(Y_k)$ is exactly

$$V_{k,v} = \alpha_{k,v}^2 \,\mathrm{Var}\left[\log_{10}(x_v)\right], \tag{13}$$

and the normalized log-space variance share is

$$S_{k,v}^{\log} = \frac{V_{k,v}}{\sum_{u \in U_k} V_{k,u}}. \tag{14}$$

This decomposition is exact for the adopted independent-input design; it is not generally valid without covariance terms when inputs are dependent.

There are no interaction terms in the additive log response. On the original mass scale, the response is multiplicative, so this statement does not imply an interaction-free mass-scale Sobol decomposition. Elasticities are exactly

$$E_{k,v} = \frac{\partial \ln M_k}{\partial \ln x_v} = \alpha_{k,v}. \tag{15}$$

They do not depend on bounds or probability distributions. For $x \sim U(a,b)$, calculate the population variance analytically using

$$\mu_{\ln x} = \frac{b\ln b - a\ln a}{b-a} - 1, \tag{16}$$

$$\mathrm{E}[(\ln x)^2] = \frac{b[(\ln b)^2 - 2\ln b + 2] - a[(\ln a)^2 - 2\ln a + 2]}{b-a}, \tag{17}$$

$$\mathrm{Var}(\log_{10} x) = \frac{\mathrm{E}[(\ln x)^2] - \mu_{\ln x}^2}{(\ln 10)^2}. \tag{18}$$

For log-uniform inputs, the variance is $[\log_{10}(b/a)]^2/12$. Finite-sample covariance is not used to define the exact B, H, HL, or HP shares.

For dependent designs, write $\Sigma = \mathrm{Cov}(\log_{10}\mathbf{x})$ and use

$$\mathrm{Var}(Y_k) = \boldsymbol{\alpha}_k^T \Sigma \boldsymbol{\alpha}_k = \sum_v \alpha_{k,v}^2 \Sigma_{vv} + 2\sum_{v<u} \alpha_{k,v}\alpha_{k,u}\Sigma_{vu}. \tag{19}$$

Covariance terms describe dependence, not nonlinear interactions in log space. The repository result tables report both marginal terms $\alpha_{k,v}^2\Sigma_{vv}/\mathrm{Var}(Y_k)$ and the explicitly chosen symmetric covariance allocation

$$A_{k,v}^{\mathrm{cov}} = \frac{\alpha_{k,v}(\Sigma\boldsymbol{\alpha}_k)_v}{\boldsymbol{\alpha}_k^T\Sigma\boldsymbol{\alpha}_k}. \tag{20}$$

The allocations sum to one, may be negative, and are neither independent Sobol indices nor causal contributions. PRCCs in restricted designs are conditional rank associations under those joint designs and can be affected by collinearity. These qualifications prevent conflating design-induced sensitivity with an invariant model property.

As variance shares are non-negative, direction was retained through

$$\tilde{S}^{\log}_{k,v} = S^{\log}_{k,v} \operatorname{sign}(\alpha_{k,v}). \tag{21}$$

For concise cross-equation screening, two summaries were defined only over equations containing input $v$:

$$G^{\mathrm{PRCC}}_{v} = \max_{k:\, v \in \mathcal{U}_k} |\mathrm{PRCC}_{k,v}|, \qquad G^{\log}_{v} = \max_{k:\, v \in \mathcal{U}_k} S^{\log}_{k,v}. \tag{22}$$

These maxima are screening summaries, not pooled sensitivity indices; equation-specific PRCCs and shares remain the primary quantities for interpretation.

### *2.5. Range Effects and Upper-Tail Profiles*

The deterministic range effect gives the signed number of output orders of magnitude induced by moving one input from its lower to its upper bound while holding the other inputs fixed:

$$\Delta^{\mathrm{range}}_{k,v} = \alpha_{k,v} \log_{10}\left(\frac{x_{v,\max}}{x_{v,\min}}\right). \tag{23}$$

Its sign gives the direction and its absolute value the magnitude. Other inputs are fixed at their geometric midpoints $\sqrt{x_{u,\min} x_{u,\max}}$; for these power laws, the log-range effect is independent of the chosen fixed values. The exact multiplicative factor is $10^{\Delta^{\mathrm{range}}_{k,v}}$. Because the calculation uses marginal endpoints, it characterizes the equation over the specified rectangular domain and need not represent a feasible one-at-a-time intervention in a real network.

For each equation, the upper-output subset was defined as the highest 5% of sampled outputs,

$$\mathcal{J}_k = \{s : M_k(s) \geq Q_{0.95}(M_k)\}, \tag{24}$$

where $s$ indexes sampled rows. For each input, the upper-tail profile was

$$U_{k,v} = \log_2\left[\frac{\mathrm{median}(x_v \mid s \in \mathcal{J}_k)}{\mathrm{median}(x_v \mid s \notin \mathcal{J}_k)}\right]. \tag{25}$$

Positive values indicate higher median inputs in high-output rows and negative values indicate lower medians. Calculation consists of sorting outputs, selecting the upper 5%, computing each input median inside and outside that subset, taking their ratio, and applying $\log_2$. The 5% threshold is descriptive and does not define a physical extreme event. These profiles describe sampled inputs; they are not causal sensitivity indices.

### *2.6. Selection Criteria and Detailed Response Diagnostics*

The equations for detailed analysis were selected after and on the basis of the global comparison. The first was the formulation showing the greatest combined departure in output magnitude, scenario ranking, and sensitivity structure. The second was the most parsimonious member of the mutually consistent group, where parsimony was defined as requiring the fewest input variables. This rule contrasts the most distinctive response with a reduced-input representative without using predictive accuracy as a criterion.

For each selected equation, four diagnostics were considered together: the output distribution, deterministic range effects, upper-tail profiles, and a two-dimensional response surface. The two surface axes were the dominant controls identified by the preceding sensitivity analysis. Inputs were evaluated on logarithmically spaced grids, and inputs

not shown on the axes were fixed at the geometric midpoint of their bounds. Contours corresponding to selected percentiles of the Monte Carlo output distribution were superimposed to connect the deterministic surface to the sampling-based output summary. These surfaces describe the response structure encoded by the empirical equations; they do not demonstrate physical mechanisms.

## 3. Results and Discussion

### *3.1. Baseline Magnitudes, Rankings, and Tail Disagreement*

Under the independent-uniform baseline B, the median outputs for EQ1–EQ4 are 34.87, 167.99, 164.46, and 159.21 kg day$^{-1}$. Figure 1 shows their induced distributions and paired differences. The paired EQ1/EQ4 median log-ratio is −0.6218, corresponding to a median paired ratio of 0.239. EQ1 is therefore lower in this design. A ratio of output medians (34.87/159.21 = 0.219) is a different statistic and should not be equated to the median paired ratio. Neither quantity establishes underprediction relative to observations.

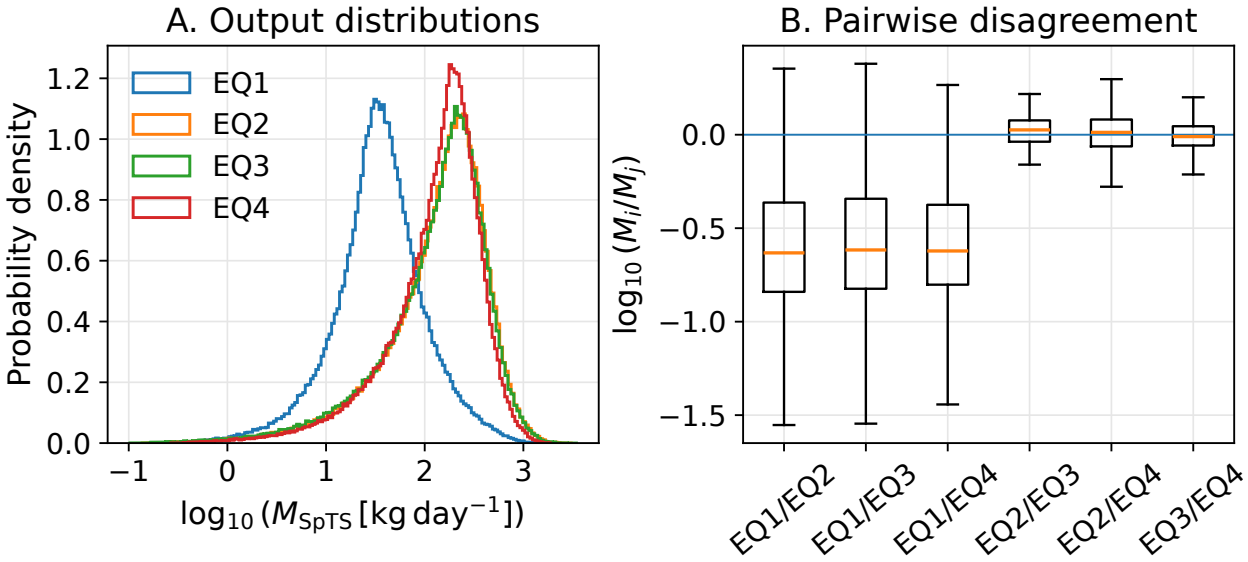



**Figure 1.** Recomputed baseline B distributions and paired log-ratios. Outputs are induced by independent-uniform synthetic inputs; the sample is an unconstrained mathematical benchmark.

EQ1 has Spearman correlations of 0.649–0.658 with EQ2–EQ4; the other pairs have correlations of 0.967–0.985 (Figure 2). Table 4 shows that strong global association conceals upper-tail disagreement. Only 21.6% of the EQ1/EQ4 top deciles coincide. Even the EQ2/EQ4 overlap is 76.2%, leaving 23.8% of each selected decile different. Thus, "highly associated" is warranted, whereas unqualified "interchangeable" is not.

Large percentile-rank shifts identify the baseline combinations that drive disagreement. EQ1 ranks 3.76% of rows at least 0.5 percentile-fraction units higher than EQ4; the reverse group contains 1.51%. Median $(S_{PD}, S)$ values are $(0.00364, 0.05566)$ in the EQ1-up group and $(0.05177, 0.00545)$ in the EQ1-down group. Median lengths are 11,663 and 25,208 m, respectively. These opposing slope combinations favor one slope regressor over the other. They are synthetic diagnostics, not observed network types, and some violate slope ordering. Their interpretation is restricted to B; the constrained comparisons below test whether separation persists after removing that inconsistency. In C, the EQ1-up and EQ1-down groups comprise 3.52% and 2.39% of retained rows; their median $(S_{PD}, S)$ values are $(0.00975, 0.05898)$ and $(0.05155, 0.00550)$. Thus, the opposing slope-regressor pattern also occurs after enforcing ordering and the density envelope. In E, the two group fractions

are 4.75% and 1.39%. Separate group summaries and the 100 largest absolute shifts for each of B, O, C, and E are supplied.

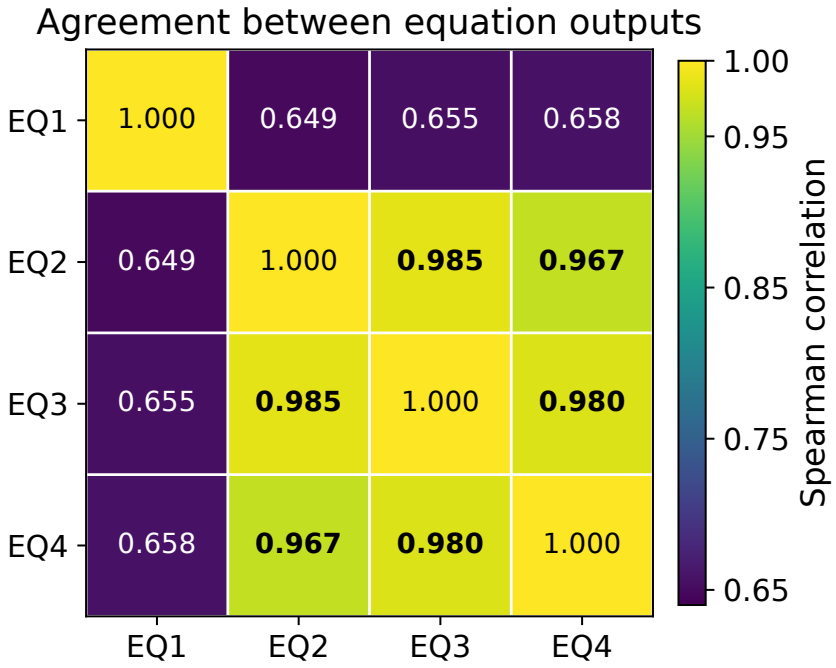



**Figure 2.** Baseline B global Spearman correlations. High global association does not guarantee agreement in magnitude or upper-tail selection.

**Table 4.** Baseline pairwise disagreement. Overlap is the percentage of one top decile shared with the other.

| Pair | Median $R_{ij}$ | $\rho_S$ | $\tau_b$ | Overlap (%) |
|---|---|---|---|---|
| EQ1/EQ2 | −0.632 | 0.649 | 0.475 | 21.6 |
| EQ1/EQ3 | −0.616 | 0.655 | 0.481 | 21.6 |
| EQ1/EQ4 | −0.622 | 0.658 | 0.484 | 21.6 |
| EQ2/EQ3 | 0.026 | 0.985 | 0.896 | 83.7 |
| EQ2/EQ4 | 0.013 | 0.967 | 0.849 | 76.2 |
| EQ3/EQ4 | −0.010 | 0.980 | 0.892 | 80.5 |

### *3.2. Elasticities, Range Effects, and Baseline Variance*

Figure 3 separates exact population log-variance shares from sample PRCCs. Under B, $L$ explains 53.2% of the EQ1 log variance and 85.2–86.8% of the EQ2–EQ4 log variance. $S_{PD}$ explains 40.4% in EQ1. These proportions combine fixed exponents with the adopted marginal ranges; they are not measurements of physical influence. Table 5 reports every nonzero exponent, exact range effect, and corresponding variance share.

The length range effect is +2.205 decades for EQ1, +3.196 for EQ2, +3.305 for EQ3, and +2.880 for EQ4. Consequently, the cross-equation range is 2.205–3.305 decades, not 2.21–2.88. The latter applies only to the selected EQ1/EQ4 comparison. Figures 4 and 5 retain that focused comparison. Their surfaces and marginal endpoint effects are mathematical slices of B; a slice need not satisfy the constraints of C or E.

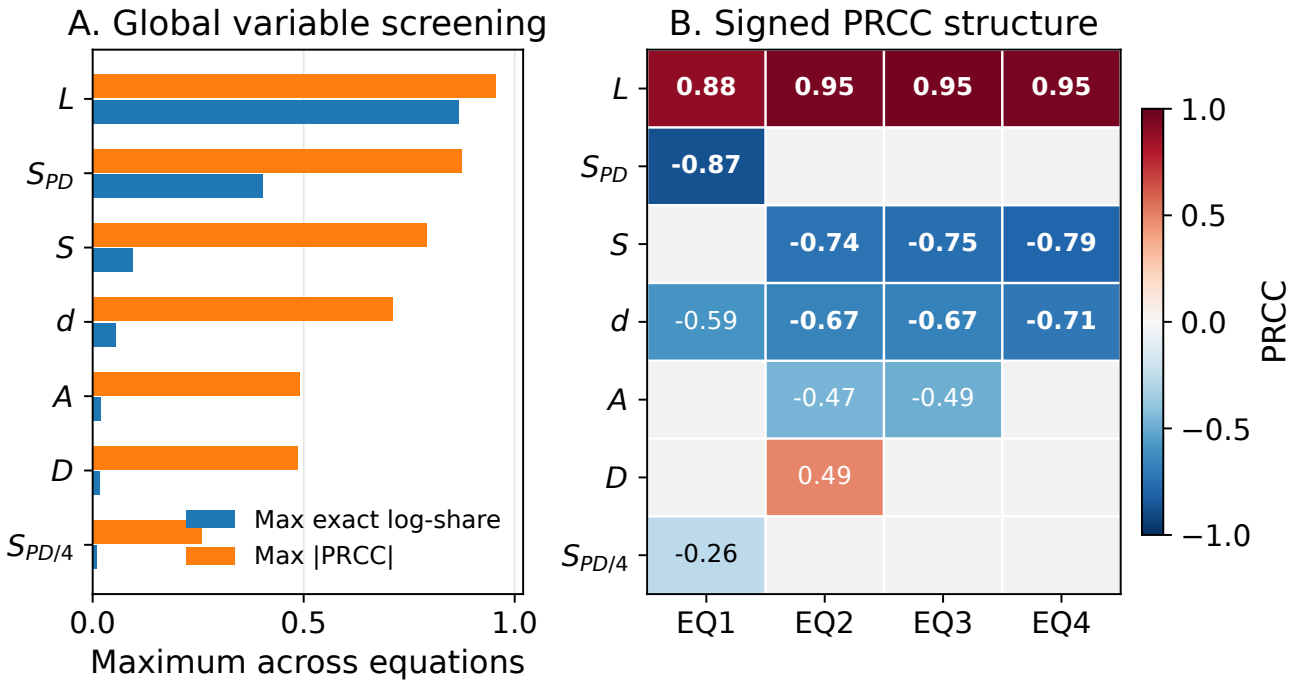



**Figure 3.** Baseline B sensitivity screening, conditional on independent-uniform historical-range inputs: cross-equation maxima of analytical independent-input log-variance shares and absolute PRCCs (**A**), and signed equation-specific PRCCs (**B**). Maxima include only equations containing the input; empty cells denote absent inputs.

The power laws encode constant elasticities. For example, a 1% local increase in $L$ corresponds approximately to 0.814% and 1.063% output increases in EQ1 and EQ4. EQ1 has a slope-descriptor elasticity of −0.819, similar in absolute magnitude to its length elasticity despite their differing baseline variance shares. This distinction explains why variance dominance cannot be interpreted without the assumed input distributions.

**Table 5.** Every nonzero elasticity, deterministic full-range effect, upper/lower output factor, and exact baseline population share. Other inputs are fixed at geometric midpoints; effects are independent of those fixed values.

| Equation | Input | $E_{k,v}$ | $\Delta^{\text{range}}$ | $10^{\Delta}$ | $S^{\log}_{k,v}$ |
|---|---|---|---|---|---|
| EQ1 | $L$ | +0.814 | +2.205 | 160.3 | 0.532 |
| EQ1 | $S_{PD}$ | −0.819 | −1.416 | 0.03839 | 0.404 |
| EQ1 | $S_{PD/4}$ | −0.108 | −0.264 | 0.5442 | 0.009 |
| EQ1 | $d$ | −0.510 | −0.415 | 0.3849 | 0.056 |
| EQ2 | $L$ | +1.180 | +3.196 | 1572 | 0.852 |
| EQ2 | $A$ | −0.178 | −0.415 | 0.3849 | 0.018 |
| EQ2 | $S$ | −0.418 | −0.638 | 0.2302 | 0.071 |
| EQ2 | $D$ | +0.604 | +0.240 | 1.739 | 0.016 |
| EQ2 | $d$ | −0.510 | −0.415 | 0.3849 | 0.043 |
| EQ3 | $L$ | +1.220 | +3.305 | 2018 | 0.868 |
| EQ3 | $A$ | −0.187 | −0.436 | 0.3667 | 0.019 |
| EQ3 | $S$ | −0.434 | −0.662 | 0.2176 | 0.072 |
| EQ3 | $d$ | −0.510 | −0.415 | 0.3849 | 0.041 |
| EQ4 | $L$ | +1.063 | +2.880 | 757.8 | 0.852 |
| EQ4 | $S$ | −0.438 | −0.668 | 0.2146 | 0.095 |
| EQ4 | $d$ | −0.510 | −0.415 | 0.3849 | 0.052 |

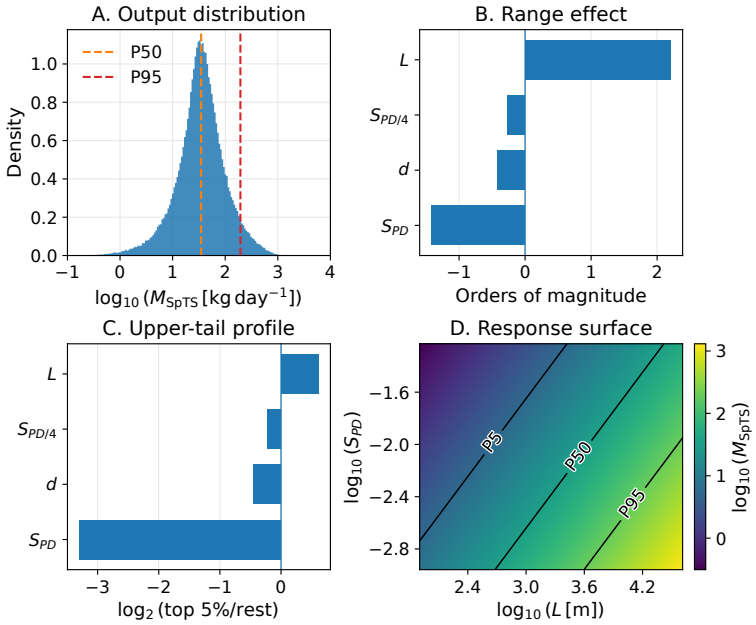



**Figure 4.** EQ1 diagnostics conditional on baseline B. (**A**) Blue histogram: induced log-output density; orange and red vertical lines: P50 and P95. (**B**) Signed endpoint effect $\alpha_v \log_{10}(b_v/a_v)$: positive values mean increasing output as the input moves from its minimum to maximum; negative values mean decreasing output. (**C**) $\log_2$ of the input median in the upper 5% of synthetic outputs divided by its median in the remaining 95%: positive values indicate a higher upper-tail input median; negative values indicate a lower one. The subset denotes upper-tail synthetic scenarios, not physical rarity. (**D**) The response surface fixes $S_{PD/4}$ and $d$ at geometric midpoints; contours show baseline 5th, 50th, and 95th log-output percentiles. This rectangular surface is not a physical intervention or an endogenous-input reconstruction.

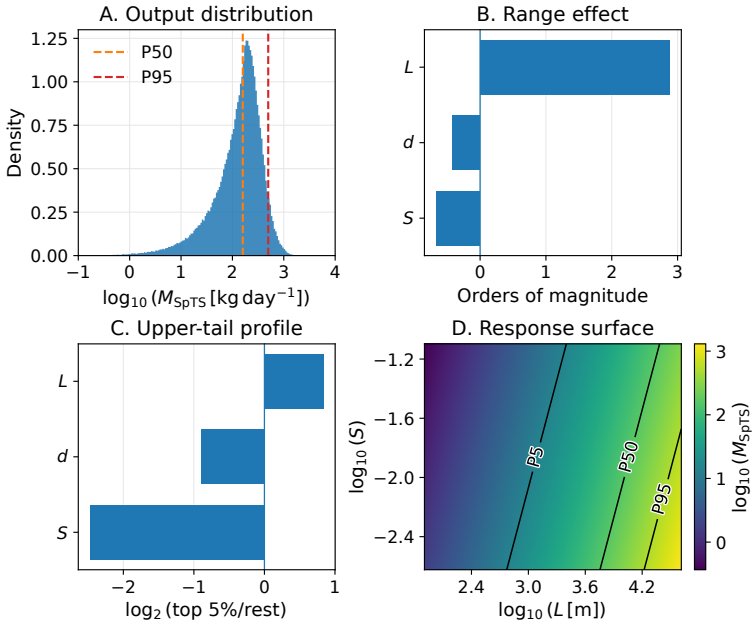



**Figure 5.** EQ4 diagnostics conditional on baseline B. (**A**) Blue histogram: induced log-output density; orange and red lines: P50 and P95. (**B**) Positive endpoint effects indicate an output increase from the input minimum to maximum; negative effects indicate a decrease, in base-10 decades. (**C**) Positive $\log_2$ upper-5%/remaining-95% input-median ratios indicate higher input medians in upper-tail synthetic scenarios; negative $\log_2$ ratios indicate lower medians. These subsets do not imply real-world rarity. (**D**) The response surface fixes $d$ at its geometric midpoint; contours show baseline 5th, 50th, and 95th log-output percentiles.

### *3.3. Ordering, Joint Constraints, and Bounds Robustness*

In B, 19.7% of rows violate $S_{PD/4} \leq S_{PD}$. This invalidates treating the baseline ensemble as a population of real sewer networks, although its positive-input evaluations are mathematically well-defined. Designs O, C, and E enforce ordering. C and E also induce substantial length–area association ($\rho_S \simeq 0.56$) through the field-informed density envelope; E links slope descriptors and mean slope ($\rho_S(S, S_{PD}) = 0.372$). Table 6 reports the resulting output and ranking changes.

**Table 6.** Design robustness ($N = 200{,}000$ per design). B: independent uniform; F: four historical flow levels; O: ordered slopes; C: order and density; E: exponential quantiles and density; H: all log-widths halved; HL: length only; HP: descriptor only; G: log-uniform. Median masses are in kg day$^{-1}$. The final three columns compare EQ1/EQ4.

| Design | $M_1$ | $M_2$ | $M_3$ | $M_4$ | $R_{14}$ | $\rho_{14}$ | $O_{14}^{(10)}$ (%) |
|---|---|---|---|---|---|---|---|
| B | 34.9 | 168.0 | 164.5 | 159.2 | −0.622 | 0.658 | 21.6 |
| F | 36.4 | 172.7 | 168.8 | 162.8 | −0.622 | 0.685 | 26.0 |
| O | 30.1 | 168.1 | 164.9 | 159.3 | −0.688 | 0.749 | 28.7 |
| C | 32.8 | 172.0 | 167.6 | 174.1 | −0.711 | 0.636 | 25.5 |
| E | 67.6 | 179.9 | 175.4 | 182.2 | −0.422 | 0.591 | 35.6 |
| H | 26.7 | 50.7 | 49.0 | 48.5 | −0.228 | 0.734 | 26.7 |
| HL | 10.2 | 28.0 | 25.8 | 31.7 | −0.466 | 0.614 | 20.8 |
| HP | 70.9 | 168.0 | 164.5 | 159.2 | −0.313 | 0.750 | 29.8 |
| G | 20.2 | 22.4 | 21.2 | 21.9 | −0.035 | 0.825 | 46.2 |

EQ1/EQ4 divergence survives these particular restricted tests: their Spearman correlations are 0.749, 0.636, and 0.591 in O, C, and E. However, the paired log-ratio is not invariant, moving from −0.622 in B to −0.688, −0.711, and −0.422. EQ2–EQ4 retain global rank agreement above 0.968 in C and E but still do not have identical upper tails (complete pairs are supplied). These restricted tests support a structural distinction conditional on their assumptions, not a universal fourfold difference.

Dependence also changes sensitivity attribution. In C, the EQ1 covariance allocations for $L$ and $S_{PD}$ are 0.421 and 0.407; in E, they are 0.198 and 0.665. The slope descriptor, rather than length, dominates EQ1 in E under this allocation. EQ4's length allocation falls from its independent-population share 0.852 in B to approximately 0.674 in C and E. The EQ1 PRCCs for $(L, S_{PD})$ are $(0.897, -0.872)$ in C and $(0.878, -0.636)$ in E; the EQ4 PRCCs for $(L, S)$ are $(0.938, -0.845)$ and $(0.944, -0.864)$. Association signs persist, but their strengths and variance allocations do not. No independent-input decomposition is applied to these dependent designs.

Table 7 reports the exact independent-uniform variance shares for the alternative bounds.

**Table 7.** Exact independent-uniform population variance shares under bounds changes. H, HL, and HP are unconstrained diagnostics.

| Design | EQ1: $L$ | EQ1: $S_{PD}$ | EQ4: $L$ | EQ4: $S$ |
|---|---|---|---|---|
| B | 0.532 | 0.404 | 0.852 | 0.095 |
| H | 0.629 | 0.329 | 0.908 | 0.065 |
| HL | 0.394 | 0.522 | 0.767 | 0.150 |
| HP | 0.703 | 0.211 | 0.852 | 0.095 |

Narrowing only the length interval (HL) changes EQ1's exact shares from $(0.532, 0.404)$ for $(L, S_{PD})$ to $(0.394, 0.522)$: the ranking reverses. Narrowing only the descriptor interval (HP) instead increases the length share to 0.703. These tests isolate the role of bounds without changing elasticities. Under G, medians become 20.19, 22.37, 21.18, and 21.88 kg day$^{-1}$, and the EQ1/EQ4 paired log-ratio is only $-0.035$. This near-convergence demonstrates that the baseline scale separation is induced jointly by equations and marginal assumptions; it is not an invariant offset between formulations. G is an unconstrained diagnostic, not evidence of predictive agreement in real networks.

Design F retains the original four wastewater-flow levels with equal weights while preserving the other six baseline columns. Its median daily deposited-solids masses are 36.4, 172.7, 168.8, and 162.8 kg day$^{-1}$ for EQ1–EQ4, respectively. The EQ1/EQ4 Spearman correlation becomes 0.685, and the top-decile overlap becomes 26.0%, compared with 0.658 and 21.6% in B. Since the same $d^{-0.510}$ factor appears in every equation, each same-row pairwise log-ratio cancels $d$ exactly: the paired $R_{14}$ median remains $-0.622$. Individual-equation rankings and variance shares can nevertheless change. Under F, the exact length shares become 0.502, 0.816, 0.833, and 0.808, while the flow shares become 0.108, 0.083, 0.080, and 0.102. This comparison supports conditional equation-group alignment without treating interpolation between historical flow levels as an observed flow distribution (Appendix C).

### *3.4. Field Context, Operational Interpretation, and Limitations*

A direct comparison of synthetic total-load medians with deposits recovered in field cleaning would mix network scale, antecedent accumulation, and maintenance. For context, we evaluated EQ4 on the eight published networks of Trapote and Egea [9]. Their listed flow is $d = 0.149$, their slopes span 0.0006–0.0113, and their lengths span 2639–91,725 m. Some inputs are outside our baseline bounds, so these calculations are explicitly external-domain context, not an in-range validation. Uncorrected EQ4 outputs span 147–5619 kg day$^{-1}$; unit outputs span 0.0241–0.0948 kg m$^{-1}$ day$^{-1}$.

That study's fitted field unit-load curve, $0.0742S^{-0.509}$ (its Equation (8)), evaluates to 0.727–3.238 in the authors' reported unit-load convention over the listed slopes. These are values of a published fit, not digitized individual measurements. The eight-network calculation is supplied as `field_context.csv`. The paper reports that maintenance and dry-period corrections materially reduce the field discrepancy. Accordingly, the 35–168 kg day$^{-1}$ baseline medians cannot establish empirical plausibility for arbitrary systems. A matched assessment needs the same network, deposit definition, mass basis, and accumulation interval; recovered sediment masses should not be relabeled as independently measured instantaneous daily deposition rates.

Within the assumed designs, EQ4 is the most parsimonious representative of the internally aligned EQ2–EQ4 group for preliminary mathematical screening, pending external validation. Its lower input burden and strong sampled association do not establish operational preference. These properties do not show that area and diameter data have no operational value or that EQ4 is an equivalent design tool. EQ1 instead requires prior model-based deposition information: its distinct response cannot be offered as a geometry-only alternative.

Any physical interpretation of positive length elasticity is a hypothesis about system extent and sediment-storage opportunity, not a finding that total length controls deposition in operating sewers. Local bottlenecks, particle properties, bed state, hydraulic stress, and antecedent dry periods may govern observed accumulation [1,2,25]. The equations do not resolve those processes. Normalizing total load by length also changes the EQ4 length elasticity from 1.063 to 0.063, further separating an extensive network total from local deposition propensity.

The omitted processes give concrete reasons to restrict extrapolation. Particle-size distributions influence settling and transport thresholds, while organic cohesion, biofilm formation, and sediment aging alter bed resistance even at similar network-average slopes [6,10,11]. Local shear, pipe cross-section, and pre-existing beds affect transport capacity and obstruction; intermittent discharges alter the sequence of settling and remobilization [13,25]. Contemporary networks with different sediment sources, maintenance histories, or wastewater composition may therefore depart from clean-pipe historical model behavior [12,16]. These mechanisms are absent from the audited regressors, and aggregate length or slope cannot be assumed to proxy them reliably.

An appropriate external validation dataset would pair independently measured dry-weather deposition over known accumulation intervals with the same networks' segment lengths, areas, diameters, slopes, and full length-weighted slope distributions, together with per-capita flow and infiltration. It would document cleaning dates and initial bed condition, antecedent dry periods and intermittent inputs, particle-size distribution, organic fraction, density, cohesion, and relevant shear conditions. Recovered wet mass, dry mass, and total-solids definitions must be reconciled, with measurement uncertainty and repeat observations across network classes reported. Local bed-depth measurements can support this effort [14,15], but conversion to network-wide daily mass requires coverage, bulk-density, and accumulation-time information. EQ1 additionally requires independent prior deposition information or an independently specified method of estimating $P_{LD}$; deriving it from the same held-out target deposits would leak validation information. Calibration or adaptation data should therefore be separated from the final evaluation networks and periods.

Limitations remain substantive: coefficients describe historical model-generated clean-pipe loads; parameter uncertainty is not propagated; synthetic uniform or log-uniform marginals are not fitted field distributions; C and E implement selected aggregate constraints rather than full hydraulic admissibility; E does not reconstruct deposition-derived $P_{LD}$; and the field-context comparison does not validate any formulation. Conclusions are therefore restricted to the equations and fully specified experimental designs. Predictive model selection requires a matched contemporary field or independently validated process-model dataset.

## 4. Conclusions

Under the independent-uniform historical-range benchmark, EQ1 gives lower daily deposited-solids masses and different scenario rankings from EQ2–EQ4. Ordering, density, and linked-quantile tests retain a distinction under their specified constraints, but its size changes. Output distributions, variance shares, and rank diagnostics remain conditional on the selected input measure; they are not real-network probabilities or physical control estimates.

EQ2–EQ4 are strongly aligned in the tested designs without being mathematically equivalent or selecting identical upper tails. EQ4 is their most parsimonious representative for preliminary mathematical screening, whereas EQ1 requires prior deposition-model information. These findings do not establish predictive superiority or operational preference. Such decisions require contemporary, independently measured, and consistently defined deposition data.

**Author Contributions:** Conceptualization, J.B.M., F.J.M.-R., J.M.P.C., and J.M.-P.; methodology, J.B.M. and F.J.M.-R.; software, J.B.M. and F.J.M.-R.; validation, J.B.M., F.J.M.-R., J.M.P.C., and J.M.-P.; formal analysis, J.B.M. and F.J.M.-R.; investigation, J.B.M.; resources, J.M.P.C. and J.M.-P.; data curation, J.B.M. and F.J.M.-R.; writing—original draft preparation, J.B.M. and F.J.M.-R.; writing—review and editing, all authors; visualization, J.B.M. and F.J.M.-R.; supervision, J.M.P.C. and J.M.-P.; project administration, J.M.-P. All authors have read and agreed to the published version of the manuscript.

**Funding:** This research received no external funding.

**Institutional Review Board Statement:** Not applicable.

**Informed Consent Statement:** Not applicable.

**Data Availability Statement:** The complete procedural Python code for the equations, sampling designs, numerical diagnostics, and figures is publicly available at https://github.com/ejose5400-design/pisano-equations-reproducibility (accessed on 27 October 2026). The repository includes fixed random seeds, dependency versions, reference CSV tables, and generated results. The code snapshot accompanying this revision is identified by https://github.com/ejose5400-design/pisano-equations-reproducibility/tree/846c3459ca3a19282bf3f7a0ad41ea423abfee75 (accessed on 27 October 2026). Appendix E describes the one-command reproduction and comparison with the manuscript reference results. The audit uses published equations and synthetic inputs; the field-context calculation uses published network descriptors and a fitted curve, rather than a new observational dataset.

**Acknowledgments:** During the preparation of this manuscript, the authors used OpenAI ChatGPT (Sol 6.1 model) for language editing, LaTeX formatting, and assistance with software development. The authors reviewed and edited the output and take full responsibility for the content of this publication.

**Conflicts of Interest:** The authors declare no conflicts of interest.

## Appendix A. Construction of the EQ1 Descriptors

Let $L$ be the sum of sewer-segment lengths. The historical procedure first obtains a cumulative deposited-mass versus cumulative pipe-length relationship from prior deposition-model output. The length fraction at 80% of the total modeled deposited mass is $p = P_{LD}/100$, and the corresponding length is $L_{PD} = pL$. Independently, pipe-slope and segment-length data define the length-weighted cumulative slope distribution $F_S(s)$. The descriptors are read from this distribution as

$$S_{PD} = F_S^{-1}(p), \qquad S_{PD/4} = F_S^{-1}(p/4). \tag{A1}$$

Interpolation can be used for empirical cumulative distributions; the quantile convention must be specified when implementing that procedure on a network. The schematic illustrates the information pathway, not a new calibration dataset. Its illustrative exponential curve is not evidence that real pipe-slope distributions are exponential. Design E only links possible quantiles to a common slope distribution; it does not generate deposition-model output or recover the endogenous $P_{LD}$.

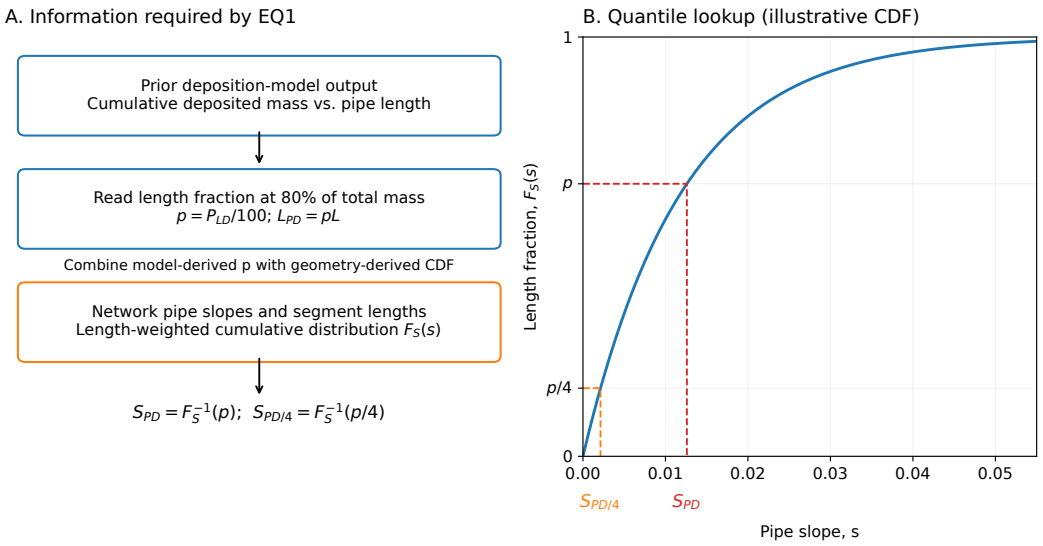



**Figure A1.** Information required by EQ1. Blue boxes identify prior model-derived deposition information; the orange box identifies geometry-derived information. The illustrative CDF shows why $S_{PD/4} \leq S_{PD}$. Its $p = 0.65$ is chosen only for illustration and does not represent measured deposition.

## Appendix B. US Customary Equations and Coefficient Conversion

### *Appendix B.1. Conventions and Source Precision*

The historical US formulations are reported by Pisano and Queiroz [4], Sections 4.5.3 and 5.2. Written at the *same rounded exponent precision audited in the manuscript*, their US customary forms are

$$T_1 = 0.0038\, L_{ft}^{0.814} S_{PD}^{-0.819} S_{PD/4}^{-0.108} q_{gal}^{-0.510}, \tag{A2}$$

$$T_2 = 0.001303\, L_{ft}^{1.180} A_{ac}^{-0.178} S^{-0.418} D_{in}^{0.604} q_{gal}^{-0.510}, \tag{A3}$$

$$T_3 = 0.00389\, L_{ft}^{1.220} A_{ac}^{-0.187} S^{-0.434} q_{gal}^{-0.510}, \tag{A4}$$

$$T_4 = 0.0076\, L_{ft}^{1.063} S^{-0.438} q_{gal}^{-0.510}. \tag{A5}$$

Here, $T_k$ is in lb day$^{-1}$; $L_{ft}$, $A_{ac}$, and $D_{in}$ are in ft, acres, and inches; $q_{gal}$ is in US gal person$^{-1}$ day$^{-1}$; slopes are dimensionless. These expressions document the historical functional forms and coefficients under the manuscript's exponent convention. They are not a verbatim transcription of every extra decimal in the original report: for example, that report prints 1.2195, −0.1866, and −0.4343 in the area-based model and −0.4375 in the simplest model. Exponents must be kept identical on both sides of a unit-conversion test. Changing exponent precision is a change to the audited equation and is not a unit conversion.

### *Appendix B.2. Worked EQ4 Conversion*

Use $L_{ft} = L/0.3048$, $q_{gal} = d/0.003785411784$, and $M_{kg} = 0.45359237\, T_{lb}$. With exponent −0.438 as audited,

$$\begin{aligned} C_{4,SI}^{conv} &= 0.45359237(0.0076)(1/0.3048)^{1.063}(1/0.003785411784)^{-0.510} \\ &= 0.0007092659707 \quad \text{(approximately)}. \end{aligned} \tag{A6}$$

The retained audited coefficient is 0.000709. Their relative difference is explicitly reported in the main coefficient table. The same transformation is implemented for all four equations in `extra_checks.py`. Historical coefficients and reconstructed SI coefficients are distinguished from the fixed rounded SI coefficient vector used for the main audit.

*Appendix B.3. Same Physical Input in Both Unit Systems*

The test uses the lower corner, geometric midpoint, and upper corner of all seven positive input intervals. Every SI input is multiplied by its exact US-per-SI factor before evaluation in the US equation. The US mass is then multiplied by 0.45359237; the SI equation is evaluated using the consistently reconstructed coefficient. All 12 comparisons agree to a maximum relative difference of $1.56 \times 10^{-15}$. The lower and upper corners are mathematical test vectors, not certified physical networks or extrema of the output. Complete inputs and outputs are in `US_SI_test_inputs.csv` and `US_SI_crosscheck.csv`.

The geometric-midpoint SI input vector, in the order of Table 3, is

$$\mathbf{x}_{gm} = (1812.9785,\ 17.745886,\ 0.013789924,\ 0.32128741,\ 0.0080492236,\ 0.0014886571,\ 0.38601539).$$

The separate rounded-coefficient discrepancy is constant over inputs. Its maximum is 0.23754% relative to reconstructed output (EQ2), equivalent to 0.238% with the main table's denominator.

**Table A1.** Geometric-midpoint US–SI identity check. The last column deliberately uses the fixed audited coefficient instead of the reconstructed coefficient; it therefore need not equal the preceding columns.

| | US Result lb/day | US Result Converted kg/day | Reconstructed SI kg/day | Audited SI kg/day |
|---|---|---|---|---|
| EQ1 | 44.49610911 | 20.18309558 | 20.18309558 | 20.19727832 |
| EQ2 | 49.59231579 | 22.49469605 | 22.49469605 | 22.44126223 |
| EQ3 | 46.85324107 | 21.25227266 | 21.25227266 | 21.22980151 |
| EQ4 | 48.25233365 | 21.88689038 | 21.88689038 | 21.87868292 |

## Appendix C. Four-Level Wastewater-Flow Sensitivity Test

F uses the baseline seven-dimensional LHS with $N = 200{,}000$ and seed 123. The six non-flow columns are exactly retained. If $u_d$ is the seventh unit-cube coordinate, set $j = \min(\lfloor 4u_d \rfloor, 3)$ and select the corresponding member of $(40, 110, 190, 260)$ US gal person$^{-1}$ day$^{-1}$. Each receives exactly 50,000 rows. The equal probabilities represent the historical experimental levels, not a fitted field distribution. This design remains independent in its target distribution, but its discrete flow column is no longer a continuous LHS marginal.

**Table A2.** Flow levels converted without rounding before evaluation.

| US Gal/Person/Day | $m^3$/Person/Day | Number of Rows |
|---|---|---|
| 40 | 0.15141647136 | 50,000 |
| 110 | 0.41639529624 | 50,000 |
| 190 | 0.71922823896 | 50,000 |
| 260 | 0.98420706384 | 50,000 |

**Table A3.** Conditional output medians (kg/day) and selected rank diagnostics in B and F.

| Design | EQ1 | EQ2 | EQ3 | EQ4 | $\rho_{14}$ | $\text{Overlap}_{14}$ |
|---|---|---|---|---|---|---|
| B | 34.871 | 167.992 | 164.462 | 159.213 | 0.6578 | 0.21635 |
| F | 36.369 | 172.736 | 168.830 | 162.786 | 0.6853 | 0.26000 |

For every paired row, $\log_{10}(M_i/M_j)$ cancels the common term $-0.510 \log_{10}(d)$ exactly, so all six paired log-ratio arrays are unchanged apart from floating-point rounding (maximum difference $8.89 \times 10^{-16}$). This cancellation does not imply that an individual equation

ranks all rows identically after changing flow. Thus, $R_{14}$ retains median −0.621807, while correlations and tail memberships change. Full pairwise, PRCC, and variance results are provided in the five `flow_*` CSV files.

For exact variance attribution, retain the six continuous-uniform log variances and replace the flow log variance with

$$V_{\log d,F} = \frac{1}{4}\sum_{j=1}^{4}\left[\log_{10}(d_j) - \frac{1}{4}\sum_{h=1}^{4}\log_{10}(d_h)\right]^2. \quad \text{(A7)}$$

Insert this population variance into the manuscript's independent log-share formula. No interaction terms arise in the log response. Length shares become 0.50225, 0.81607, 0.83254, and 0.80773 for EQ1–EQ4; flow shares become 0.10795, 0.08347, 0.07966, and 0.10180. The distinction between invariant exponents and distribution-dependent attribution is therefore consequential even within the historical four-level support.

## Appendix D. Sample-Size and Seed Convergence

One common seven-column independent-uniform LHS is generated separately for each sample size and seed. These are independent replications by design size, not a nested sequence. The table reproduces the repository file `convergence.csv`; seed ranges are numerical stability checks, not field uncertainty or confidence intervals. At $N = 200{,}000$, medians span 34.871–34.935 for EQ1 and 158.876–159.242 for EQ4; $\rho_{14}$ spans 0.65778–0.65929; and overlap spans 0.21635–0.22470. These checks support the precision of the reported rounded summaries for this design, while tail overlap remains visibly more seed-sensitive than median mass. They do not establish convergence of every possible statistic or certify the physical plausibility of the input distribution.

**Table A4.** All sample-size/seed checks for the unconstrained baseline. Medians are in kg/day; overlap is the intersection divided by one top-decile size.

| $N$ | Seed | Median EQ1 | Median EQ4 | Spearman$_{14}$ | Overlap$_{14}$ |
|---|---|---|---|---|---|
| 10,000 | 123 | 34.877 | 159.186 | 0.66111 | 0.22600 |
| 10,000 | 124 | 34.818 | 159.718 | 0.65084 | 0.22500 |
| 10,000 | 125 | 34.600 | 157.748 | 0.66031 | 0.23400 |
| 50,000 | 123 | 34.815 | 159.275 | 0.65782 | 0.22140 |
| 50,000 | 124 | 34.933 | 159.922 | 0.65845 | 0.22140 |
| 50,000 | 125 | 34.938 | 159.296 | 0.65899 | 0.21400 |
| 200,000 | 123 | 34.871 | 159.213 | 0.65778 | 0.21635 |
| 200,000 | 124 | 34.935 | 159.242 | 0.65929 | 0.22470 |
| 200,000 | 125 | 34.922 | 158.876 | 0.65850 | 0.22155 |

## Appendix E. Computational Reproducibility

The public repository uses procedural functions and arrays, with no user-defined classes. The roles of the source files are separated for readability: `model.py` defines the units, equations, input designs, and diagnostics; `plots.py` produces Figures 1–5 and A1; `extra_checks.py` performs the four-level flow and conversion checks; and `verify_results.py` compares regenerated numerical tables with the stored manuscript reference results. The entry script `reproduce.py` calls this complete workflow.

With Python 3.12 and the pinned packages in `requirements.txt`, run from the code directory:

```
python -m pip install -r requirements.txt
python reproduce.py
```

The default experiment retains all 200,000 rows per design and the declared seeds; it does not silently reduce the sample size. Outputs include the CSV tables, software and numerical-check manifests, Figures 1–5 in PDF/SVG/600-dpi PNG, and the Appendix A schematic. The optional `--figures-only` flag regenerates the figures from the baseline design without recomputing the additional design tables; `--save-samples` also writes the regenerable NPZ matrices. The latter are omitted from the public-code package to reduce its size.

The numerical verification checks every reference CSV's dimensions, labels, and values, with relative tolerance $10^{-10}$ and absolute tolerance $10^{-12}$ for floating-point columns. A mismatch stops the workflow; passing comparisons are recorded in `verification_report.json`. This checks numerical reproduction of the synthetic experiment, not predictive accuracy against observations. PDF/SVG container metadata can differ across runs without changing the figures. Fixed plotting parameters preserve the original palette and the P50/P95 markers described in the main captions.

The public repository, https://github.com/ejose5400-design/pisano-equations-reproducibility (accessed on 27 October 2026), includes a README, dependency versions, reference result tables, citation metadata, and a code license. The source snapshot for this revision is https://github.com/ejose5400-design/pisano-equations-reproducibility/tree/846c3459ca3a19282bf3f7a0ad41ea423abfee75 (accessed on 27 October 2026) (accessed on 27 October 2026). Methods, derivations, numerical conversion checks, and convergence evidence appear in Appendices A–D of this same article.

## References


1. Ashley, R.M.; Crabtree, B.; Fraser, A.; Hvitved-Jacobsen, T. European Research into Sewer Sediments and Associated Pollutants and Processes. *J. Hydraul. Eng.* **2003**, *129*, 267–275. [CrossRef]
2. Fan, C.Y. *Sewer Sediment and Control: A Management Practices Reference Guide*; Technical Report EPA/600/R-04/059; U.S. Environmental Protection Agency, National Risk Management Research Laboratory: Edison, NJ, USA, 2004.
3. Ashley, R.M.; Fraser, A.; Burrows, R.; Blanksby, J. The Management of Sediment in Combined Sewers. *Urban Water* **2000**, *2*, 263–275. [CrossRef]
4. Pisano, W.C.; Queiroz, C.S. *Procedures for Estimating Dry Weather Pollutant Deposition in Sewerage Systems*; Technical Report EPA-600/2-77-120; U.S. Environmental Protection Agency, Municipal Environmental Research Laboratory: Cincinnati, OH, USA, 1977.
5. Ashley, R.M.; Bertrand-Krajewski, J.L.; Hvitved-Jacobsen, T. Sewer Solids—20 Years of Investigation. *Water Sci. Technol.* **2005**, *52*, 73–84. [CrossRef]
6. Seco, I.; Gómez-Valentín, M.; Schellart, A.N.A.; Tait, S.J. Erosion Resistance and Behaviour of Highly Organic In-Sewer Sediment. *Water Sci. Technol.* **2014**, *69*, 672–679. [CrossRef]
7. Pisano, W.C.; Aronson, G.L.; Queiroz, C.S.; Blanc, F.C.; O'Shaughnessy, J.C. *Dry-Weather Deposition and Flushing for Combined Sewer Overflow Pollution Control*; Technical Report EPA-600/2-79-133; U.S. Environmental Protection Agency, Municipal Environmental Research Laboratory: Cincinnati, OH, USA, 1979.
8. Pisano, W.C.; Queiroz, C.S.; Aronson, G.L.; Blanc, F.C.; O'Shaughnessy, J.C. Procedures for Estimating Dry Weather Pollutant Deposition in Sewer Systems. *J. Water Pollut. Control Fed.* **1981**, *53*, 1627–1636.
9. Trapote, A.; Egea, R. Sediment Load Estimation in Combined Sewer Systems Located in Semi-Arid Areas: A Case Study. In *Proceeding of the Sustainable City XI*; WIT Transactions on Ecology and the Environment; WIT Press: Southampton, UK, 2016; Volume 204, pp. 777–788. [CrossRef]
10. Regueiro-Picallo, M.; Suárez, J.; Sañudo, E.; Puertas, J.; Anta, J. New insights to study the accumulation and erosion processes of fine-grained organic sediments in combined sewer systems from a laboratory scale model. *Sci. Total Environ.* **2020**, *716*, 136923. [CrossRef]
11. Tang, Z.; Xu, H.; Zhu, R.; Li, D.; Zhao, Z.; Xiao, H.; Li, H. Long-term effects of food waste on erosion resistance and production of methane and sulfide in sewer sediments: New insights into extracellular polymeric substances and genetic response mechanisms. *J. Environ. Manag.* **2025**, *377*, 124700. [CrossRef]
12. Liu, L.; Kawaike, K.; Wada, K.; Koshiba, T.; Chen, X.; Han, C.; Matsui, H. Environmental drivers of sediment accumulation in urban sewer systems: A case study of Kyoto City, Japan. *Water Res.* **2025**, *268*, 122721. [CrossRef]

13. Yang, Z.; Huang, B.; Zhu, D.Z. Quantifying Sediment Deposition in Sewers through Hydraulic Performance Analysis. *Water Sci. Technol.* **2025**, *91*, 1058–1076. [CrossRef]
14. Regueiro-Picallo, M.; Anta, J.; Naves, A.; Figueroa, A.; Rieckermann, J. Towards urban drainage sediment accumulation monitoring using temperature sensors. *Environ. Sci. Water Res. Technol.* **2023**, *9*, 3200–3212. [CrossRef]
15. Regueiro-Picallo, M.; Schellart, A.; Jensen, H.; Langeveld, J.; Viklander, M.; Lundy, L. Flow rate influence on sediment depth estimation in sewers using temperature sensors. *Water Sci. Technol.* **2024**, *89*, 3133–3146. [CrossRef]
16. Ribalta Gené, M.; Béjar, R.; Mateu, C.; Corominas, L.; Esbrí, O.; Rubión, E. Sewer sediment deposition prediction using a two-stage machine learning solution. *J. Hydroinform.* **2024**, *26*, 727–743. [CrossRef]
17. McKay, M.D.; Beckman, R.J.; Conover, W.J. A Comparison of Three Methods for Selecting Values of Input Variables in the Analysis of Output from a Computer Code. *Technometrics* **1979**, *21*, 239–245. [CrossRef]
18. Helton, J.C.; Davis, F.J.; Johnson, J.D. A Comparison of Uncertainty and Sensitivity Analysis Results Obtained with Random and Latin Hypercube Sampling. *Reliab. Eng. Syst. Saf.* **2005**, *89*, 305–330. [CrossRef]
19. Helton, J.C.; Johnson, J.D.; Sallaberry, C.J.; Storlie, C.B. Survey of Sampling-Based Methods for Uncertainty and Sensitivity Analysis. *Reliab. Eng. Syst. Saf.* **2006**, *91*, 1175–1209. [CrossRef]
20. Bland, J.M.; Altman, D.G. Statistical Methods for Assessing Agreement between Two Methods of Clinical Measurement. *Lancet* **1986**, *327*, 307–310. [CrossRef]
21. Spearman, C. The Proof and Measurement of Association between Two Things. *Am. J. Psychol.* **1904**, *15*, 72–101. [CrossRef]
22. Hamby, D.M. A Review of Techniques for Parameter Sensitivity Analysis of Environmental Models. *Environ. Monit. Assess.* **1994**, *32*, 135–154. [CrossRef]
23. Marino, S.; Hogue, I.B.; Ray, C.J.; Kirschner, D.E. A Methodology for Performing Global Uncertainty and Sensitivity Analysis in Systems Biology. *J. Theor. Biol.* **2008**, *254*, 178–196. [CrossRef]
24. Saltelli, A.; Ratto, M.; Andres, T.; Campolongo, F.; Cariboni, J.; Gatelli, D.; Saisana, M.; Tarantola, S. *Global Sensitivity Analysis: The Primer*; John Wiley & Sons: Chichester, UK, 2008. [CrossRef]
25. Butler, D.; May, R.; Ackers, J. Self-Cleansing Sewer Design Based on Sediment Transport Principles. *J. Hydraul. Eng.* **2003**, *129*, 276–282. [CrossRef]


**Disclaimer/Publisher's Note:** The statements, opinions and data contained in all publications are solely those of the individual author(s) and contributor(s) and not of MDPI and/or the editor(s). MDPI and/or the editor(s) disclaim responsibility for any injury to people or property resulting from any ideas, methods, instructions or products referred to in the content.